

Article

# E-Sail Optimal Trajectories to Heliostationary Points

Alessandro A. Quarta \*  and Giovanni Mengali 

Department of Civil and Industrial Engineering, University of Pisa, I-56122 Pisa, Italy

\* Correspondence: [alessandro.antonio.quarta@unipi.it](mailto:alessandro.antonio.quarta@unipi.it)

**Abstract:** The aim of this paper is to investigate the performance of a robotic spacecraft, whose primary propulsion system is an electric solar wind sail (E-sail), in a mission to a heliostationary point (HP)—that is, a static equilibrium point in a heliocentric and inertial reference frame. A spacecraft placed at a given HP with zero inertial velocity maintains that heliocentric position provided the on-board thrust is able to counterbalance the Sun’s gravitational force. Due to the finite amount of storable propellant mass, a prolonged mission toward an HP may be considered as a typical application of a propellantless propulsion system. In this respect, previous research has been concentrated on the capability of high-performance (photonic) solar sails to reach and maintain such a static equilibrium condition. However, in the case of a solar-sail-based spacecraft, an HP mission requires a sail design with propulsive characteristics that are well beyond the capability of current or near-future technology. This paper shows that a medium-performance E-sail is able to offer a viable alternative to the use of photonic solar sails. To that end, we discuss a typical HP mission from an optimal viewpoint, by looking for the minimum time trajectory necessary for a spacecraft to reach a given HP. In particular, both two- and three-dimensional scenarios are considered, and the time-optimal mission performance is analyzed parametrically as a function of the HP heliocentric position. The paper also illustrates a potential mission application involving the observation of the Sun’s poles from such a static inertial position.

**Keywords:** electric solar wind sail; heliostationary point; trajectory optimization; propellantless propulsion system; Sun’s poles observation

**Citation:** Quarta, A.A.; Mengali, G.E-Sail Optimal Trajectories to Heliostationary Points. *Aerospace* **2023**, *10*, 194. <https://doi.org/10.3390/aerospace10020194>

Academic Editor: Andris Slavinskis

Received: 25 January 2023

Revised: 12 February 2023

Accepted: 15 February 2023

Published: 17 February 2023



**Copyright:** © 2023 by the authors. Licensee MDPI, Basel, Switzerland. This article is an open access article distributed under the terms and conditions of the Creative Commons Attribution (CC BY) license (<https://creativecommons.org/licenses/by/4.0/>).

## 1. Introduction

A heliostationary point (HP) is a static equilibrium point in an inertial (heliostationary) reference frame and is characterized by a single design parameter—its distance from the Sun. In this sense, an HP is a type of application of Robert Forward’s “statite” concept [1], originally proposed to operate a spacecraft in near-Earth space for scientific observation and telecommunication purposes [2,3], extended to the more general case of a heliocentric mission case.

An HP is initially reached by steering the propulsive acceleration vector so that the spacecraft inertial velocity goes to zero at that particular point [4] and is then maintained there by balancing the Sun’s gravitational pull with the aid of a continuous-thrust system [5]. For this reason, a prolonged robotic mission toward an HP may be seen as a natural application of a propellantless propulsion system and, indeed, the scientific literature reports elegant studies involving photonic solar sails, starting from the pioneering works by Forward [1] and McInnes et al. [6].

It is known, however, that the maintenance of an HP requires a very high-performance solar sail [7,8]—that is, a sail with a reference propulsive acceleration well beyond the current or near-future technology [9,10]. The need for a high-performance solar sail is due to the fact that the solar radiation pressure, which is responsible for the sail thrust, varies with the solar distance in the same manner as the Sun’s gravitational acceleration.

As a result, an HP can only be maintained provided that the solar sail has a lightness number, defined as the ratio of the maximum sail-induced thrust to the local Sun’s

gravitational pull, equal to one. In other terms, when the Sun–HP distance is one astronomical unit, a solar sail with no degradation [11] must be able to produce a propulsive acceleration slightly below  $6 \text{ mm/s}^2$ . To give an idea on how large this value is, the design of the CubeSat solar sail used in the NASA’s Near-Earth Asteroid Scout mission (which is currently considered as lost after its deployment failure in mid November 2022) had a lightness number of 0.0106, while NASA’s Solar Cruiser, to be launched in 2025, will have a lightness number of about 0.0287 [12].

Fortunately enough, there exist other propellantless thruster concepts that do not employ the solar radiation pressure for producing a propulsive acceleration [13,14] and which allow an HP to be reached and maintained for a theoretically indefinite time interval by means of a medium-performance propulsion system. This is the case of the electric solar wind sail (E-sail) [15], an innovative propulsion concept proposed by Pekka Janhunen [16] in 2004, which converts the momentum from the solar wind charged particles into deep space thrust [17] through a grid of long charged tethers [18].

In a typical design, the thrust magnitude and the attitude of the reference plane of a spin-stabilized E-sail can be controlled by suitably varying the electric voltage of each tether [19,20]. According to the latest E-sail thrust model [21], the maximum propulsive acceleration magnitude varies with the inverse spacecraft distance from the Sun, so that an HP with a solar distance greater than one astronomical unit can be theoretically maintained with a sail lightness number below one.

The aim of this paper is to investigate the E-sail performance in a representative HP mission from an optimal viewpoint. In particular, both two- and three-dimensional mission scenarios are studied to analyze the minimum-time transfer of an E-sail-based spacecraft toward a given HP as a function of its position in a heliocentric reference frame. The paper also discusses a set of mission applications that involve observation of the Sun’s poles from a static inertial position. The proposed analysis allows the minimum flight time to be obtained in a parametric way as a function of the mission design parameters. In this sense, the numerical results presented in this paper extend the recent study of Ref. [22], which only focuses on the stability and control problem of an E-sail already placed at a prescribed HP.

The remainder of the paper is organized as follows. Section 2 describes the HP mission and introduces the mathematical model, including a brief discussion on the approach used in the trajectory optimization. Section 3 shows the numerical results obtained in a set of E-sail-based missions, with a focus on the special case of equilibrium points that are useful for the scientific observation of the Sun’s poles. Finally, the last section contains our concluding remarks.

## 2. Mission Description and Mathematical Problem Statement

Consider a spacecraft that initially (time  $t = t_0 \triangleq 0$ ) traces a heliocentric circular orbit in the ecliptic plane. Let  $r_{\oplus} \triangleq 1 \text{ au}$  be the orbital radius and introduce a spherical reference frame  $\mathcal{T}(O; r, \theta, \phi)$  with its origin  $O$  coinciding with the Sun’s center-of-mass, where  $r$  is the Sun–spacecraft distance,  $\theta$  is the ecliptic longitude, and  $\phi$  is the ecliptic latitude; see Figure 1. In the same figure,  $\hat{i}_r$  is the radial unit vector,  $\hat{i}_\theta$  is the trasverse unit vector, and  $\hat{i}_\phi$  is the azimuthal unit vector.

The ecliptic longitude  $\theta$  is measured, in the ecliptic plane counterclockwise from the  $x$ -axis of a heliocentric–ecliptic [23] reference frame  $\mathcal{T}_S(O; x, y, z)$ , while the ecliptic latitude  $\phi$  gives the inclination of the Sun–spacecraft line relative to the  $(x, y)$  plane—that is, the ecliptic; see Figure 1. The initial condition describes a simplified Earth’s heliocentric trajectory, whose orbital eccentricity is neglected, and a spacecraft that leaves the Earth’s sphere of influence with zero hyperbolic excess velocity relative to the starting planet.

The primary propulsion system of the spacecraft is an E-sail that, according to the latest thrust model [21], gives a propulsive acceleration vector

$$\mathbf{a} = \tau \frac{a_c}{2} \left( \frac{r_{\oplus}}{r} \right) [\hat{i}_r + (\hat{\mathbf{n}} \cdot \hat{i}_r) \hat{\mathbf{n}}] \quad (1)$$

where  $\tau \in \{0, 1\}$  is a switching (dimensionless) parameter that models the thruster operating mode: either on (when  $\tau = 1$ ) or off (i.e.,  $\tau = 0$ ). These two modes are obtained by switching on or off the onboard electron gun powered by the solar panels [24,25]. In Equation (1),  $a_c$  is the characteristic acceleration [26], which is defined as the maximum propulsive acceleration magnitude  $\|a\|$  at a solar distance  $r = r_{\oplus}$ , and  $\hat{n}$  is the unit vector normal to the sail nominal plane (the plane that ideally contains the charged tethers) in the direction opposite to the Sun. Note that the maximum propulsive acceleration is obtained when  $\hat{n} \equiv \hat{i}_r$ , that is, when the E-sail is in a Sun-facing condition [27,28], and the propulsion system gives a purely radial thrust. In that particular case, the spacecraft heliocentric trajectory may be described with a semi-analytical approach as thoroughly discussed in Refs. [29,30].

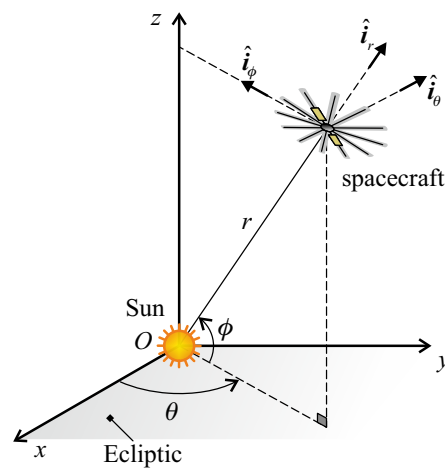


Figure 1. Reference frames and spacecraft state variables.

2.1. E-Sail Performance Requirements

The HP to be reached and maintained by the spacecraft is characterized by a given distance  $r_{HP}$  from the Sun and a prescribed ecliptic latitude  $\phi_{HP}$ . The ecliptic longitude, instead, is left free, so that the pair  $\{r_{HP}, \phi_{HP}\}$  locates a sort of “ring” of possible static equilibrium points placed at a distance  $h_{HP} = r_{HP} \sin \phi_{HP}$  from the ecliptic, as sketched in Figure 2. The special case when  $\phi_{HP} = 0$  deg coincides with an HP that lies on the ecliptic at a distance  $r_{HP}$  from the star.

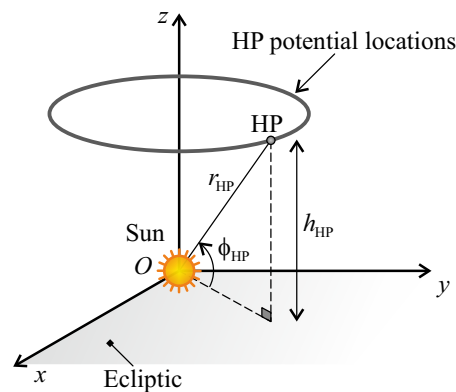


Figure 2. HP potential locations, as a function of  $\{r_{HP}, \phi_{HP}\}$ , in the heliocentric-ecliptic reference frame.

As soon as the spacecraft reaches the design HP with zero inertial velocity, it immediately assumes a Sun-facing orientation to fully exploit the available propulsive acceleration magnitude and balance the gravitational acceleration from the Sun. The latter is in the

radial direction and has a magnitude  $\mu_{\odot}/r_{\text{HP}}^2$ , where  $\mu_{\odot}$  is the Sun's gravitational parameter. Bearing in mind Equation (1), the assigned HP may be maintained with a Sun-facing attitude (i.e.,  $\hat{n} = \hat{i}_r$ ) if

$$a_c \left( \frac{r_{\oplus}}{r_{\text{HP}}} \right) = \frac{\mu_{\odot}}{r_{\text{HP}}^2} \quad (2)$$

from which the required value  $a_c^*$  of the characteristic acceleration is

$$a_c = a_c^* \triangleq \left( \frac{r_{\oplus}}{r_{\text{HP}}} \right) \left( \frac{\mu_{\odot}}{r_{\oplus}^2} \right) \quad (3)$$

Note that the ratio  $\mu_{\odot}/r_{\oplus}^2 \simeq 5.93 \text{ mm/s}^2$  coincides with the characteristic acceleration necessary for a solar-sail-based spacecraft [8] to maintain a generic HP. Therefore, according to Equation (3), a spacecraft propelled by an E-sail is potentially able to maintain a static equilibrium condition with a characteristic acceleration smaller than that required by a photonic solar sail. This aspect is better appreciated by looking at Figure 3, which shows the variation of  $a_c^*$  with the solar distance  $r_{\text{HP}}$  as modeled by Equation (3).

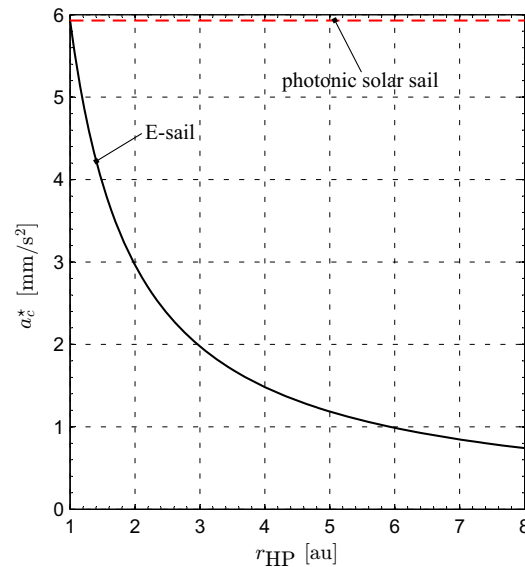


**Figure 3.** Characteristic acceleration necessary for a spacecraft to maintain an HP as a function of its solar distance  $r_{\text{HP}}$ ; see also Equation (3).

According to Figure 3, a medium-performance E-sail with a characteristic acceleration of  $1 \text{ mm/s}^2$  can maintain an HP at a distance from the Sun of roughly 6 au, while a high-performance E-sail with  $a_c = a_c^* = 3 \text{ mm/s}^2$  is able to perform an HP scientific mission at a solar distance of about 2 au. In both cases, the required characteristic acceleration is only a fraction of the value required by a solar sail (roughly 17% and 50%, respectively). For a given value of  $a_c$ , the characteristics of the E-sail propulsion system depend on the payload mass as discussed in Ref. [31]. For example, assuming a value of  $a_c = 1 \text{ mm/s}^2$  and a payload mass of 100 kg, the typical mass budget model [31] gives an E-sail with 44 tethers of 15 km each, a required electric power of about 500 W, and a total mass of slightly less than 400 kg.

Unfortunately, a higher value of the Sun–HP distance  $r_{\text{HP}}$  poses a number of technical issues, such as those related to the actual capability of the solar panels to provide the electric power necessary for the spacecraft (including the E-sail propulsion system) and for the regular working of the scientific payload. In the remainder of this section, we quantify the effect of the Sun–HP distance on the flight time necessary for the spacecraft to reach the given equilibrium point starting from the parking orbit. To this end, the spacecraft

dynamics are described in the spherical reference frame  $\mathcal{T}$ , and the transfer trajectory is obtained with an indirect approach as discussed in the next section.

2.2. Spacecraft Dynamics and Trajectory Optimization

The orientation of the normal and radial unit vectors ( $\hat{n}$  and  $\hat{i}_r$ , respectively) may be written as a function of the sail cone angle  $\alpha \in [0, \pi/2]$  rad and the sail clock angle  $\delta \in [0, 2\pi]$  rad, which are illustrated in Figure 4.

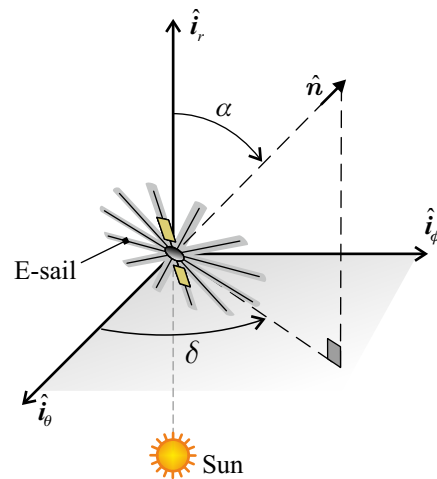


Figure 4. E-sail control angles  $\{\alpha, \delta\}$ .

According to Figure 4, the components of these unit vectors in  $\mathcal{T}(O; \hat{i}_r, \hat{i}_\theta, \hat{i}_\phi)$  are

$$[\hat{n}]_{\mathcal{T}} = \begin{bmatrix} \cos \alpha \\ \sin \alpha \cos \delta \\ \sin \alpha \sin \delta \end{bmatrix}, \quad [\hat{i}_r]_{\mathcal{T}} = \begin{bmatrix} 1 \\ 0 \\ 0 \end{bmatrix} \tag{4}$$

so that, from Equation (1), the components of the propulsive acceleration vector  $a$  in the spherical reference frame  $\mathcal{T}$  can be written as

$$[a]_{\mathcal{T}} = \begin{bmatrix} a_r \\ a_\theta \\ a_\phi \end{bmatrix} \triangleq \tau \frac{a_c}{2} \left( \frac{r_\oplus}{r} \right) \begin{bmatrix} 1 + \cos^2 \alpha \\ \cos \alpha \sin \alpha \cos \delta \\ \cos \alpha \sin \alpha \sin \delta \end{bmatrix} \tag{5}$$

From the preceding equation, the three control (scalar) variables are, therefore,  $\{\tau, \alpha, \delta\}$ , and the E-sail-based spacecraft equations of motion in  $\mathcal{T}$  are given by [32,33]

$$\dot{r} = v_r \tag{6}$$

$$\dot{\theta} = \frac{v_\theta}{r \cos \phi} \tag{7}$$

$$\dot{\phi} = \frac{v_\phi}{r} \tag{8}$$

$$\dot{v}_r = \frac{v_\theta^2 + v_\phi^2}{r} - \frac{\mu_\odot}{r^2} + a_r \tag{9}$$

$$\dot{v}_\theta = \frac{v_\theta v_\phi \tan \phi - v_r v_\theta}{r} + a_\theta \tag{10}$$

$$\dot{v}_\phi = -\frac{v_\theta^2 \tan \phi + v_r v_\phi}{r} + a_\phi \tag{11}$$

where  $\{a_r, a_\theta, a_\phi\}$  are obtained from Equation (5) as a function of the control variables, while  $\{v_r, v_\theta, v_\phi\}$  are the three components of the spacecraft (inertial) velocity vector. Without loss of generality, we assume that, at time  $t = t_0$ , the spacecraft lies along the  $x$ -axis of the  $\mathcal{T}_S(O; x, y, z)$  frame (see Figure 1) so that the initial spacecraft state variables are

$$r(t_0) = r_\oplus, \theta(t_0) = 0, \phi(t_0) = 0, v_r(t_0) = 0, v_\theta(t_0) = \sqrt{\frac{\mu_\odot}{r_\oplus}}, v_\phi(t_0) = 0 \quad (12)$$

while the final conditions (at time  $t = t_f$ ) are

$$r(t_f) = r_{\text{HP}}, \phi(t_f) = \phi_{\text{HP}}, v_r(t_f) = 0, v_\theta(t_f) = 0, v_\phi(t_f) = 0 \quad (13)$$

The time variation of the three control variables  $\tau = \tau(t)$ ,  $\alpha = \alpha(t)$ , and  $\delta = \delta(t)$  are obtained by minimizing the flight time  $\Delta t = t_f - t_0 \equiv t_f$  necessary for the spacecraft to move from the (ecliptic) circular parking orbit of radius  $r = r_\oplus$  to the HP of given geometric characteristics  $\{r_{\text{HP}}, \phi_{\text{HP}}\}$ . Note that, according to Equation (13), the final value of the ecliptic longitude is left free, so that both  $t_f$  and  $\theta(t_f)$  are two outputs of the optimization process briefly described below.

The minimum time trajectories are sought by imposing the constraint that, along the transfer trajectory, the Sun–spacecraft distance cannot be smaller than a minimum allowable perihelion radius  $r_p > 0$  or

$$r \geq r_p \quad \text{for } t \in [t_0, t_f] \quad (14)$$

The value of  $r_p$  essentially depends on the characteristics of the E-sail structure. For example, using the data reported in Ref. [34], in the rest of the paper, we assume  $r_p \triangleq 0.33$  au, a value consistent with the copper tethers employed in the E-sail structural design. The optimization process uses an indirect approach, whose main features are discussed in the classical textbook by Bryson and Ho [35]. The presence of Equation (14) implies that we are dealing with a minimum time problem with inequality (path) constraints on one of the state variables—that is, the Sun–spacecraft distance  $r$ .

In this case, the Hamiltonian function, the Euler–Lagrange equations, and the set of additional constraints required to complete the (associated) two-point boundary value problem are obtained paralleling the procedure used in Ref. [34]. In particular, the optimal control law of the switching parameter  $\tau$  and that for the sail attitude angles  $\{\alpha, \delta\}$  were derived from the general results of Huo et al. [21]. The mathematical model used in the optimization process is summarized in the Appendix A.

### 3. Numerical Simulations and Parametric Analysis

With the aid of Figure 3, which gives the required characteristic acceleration for a desired Sun–HP distance, a set of interplanetary trajectories are optimized to estimate the transfer performance of an E-sail-based spacecraft in a mission to a stationary point placed at a distance  $r_{\text{HP}} \in [2, 8]$  au from the Sun. The range of variation of the target HP distance allows the designer to appreciate how the E-sail propulsive performance influences the optimal transfer trajectory characteristics. The chosen interval of  $r_{\text{HP}}$  approximately corresponds to a characteristic acceleration  $a_c^* \in [3, 0.9]$  mm/s<sup>2</sup>, thus, including the cases of high- and medium-performance E-sails.

A preliminary trajectory analysis shows that the topology of the generic optimal transfer trajectory falls into one of the following three cases, which are illustrated in Figure 5 assuming a simplified two-dimensional scenario to facilitate the figure’s readability.

The notation of Figure 5, below described, was adapted from that introduced by the authors in Ref. [34].

1. **Direct transfer (DT).** During the optimal transfer, the Sun–spacecraft distance  $r$  continuously increases with time until the vehicle reaches the target HP, so that the

- perihelion distance of the optimal transfer coincides with the radius  $r_{\oplus}$  of the circular parking orbit; see Figure 5a.
2. **Solar wind assist with inactive perihelion constraint (iSWA).** In this case, the minimum-time transfer trajectory contains a phase where the spacecraft approaches the Sun to increase its propulsive acceleration magnitude according to the thrust model of Equation (1). Paralleling the nomenclature used for a solar sail mission case [36], this behavior can be seen as a sort of solar wind assist (SWA) because of the thrust increase due to the variation of solar wind plasma density. The approaching phase ends when the spacecraft reaches a perihelion distance  $\min(r)$  that, in this case, is greater than the minimum admissible value  $r_p = 0.33$  au, so that the inequality constraint (14) is naturally satisfied (case of inactive constraint); see Figure 5b.
  3. **Solar wind assist with active perihelion constraint (aSWA).** This case is similar to the preceding one, with the only difference that the perihelion distance of the transfer trajectory is equal to  $r_p = 0.33$  au as sketched in Figure 5c. In other terms,  $\min(r) = r_p$ , and thus the constraint (14) on the solar distance becomes active at the perihelion.

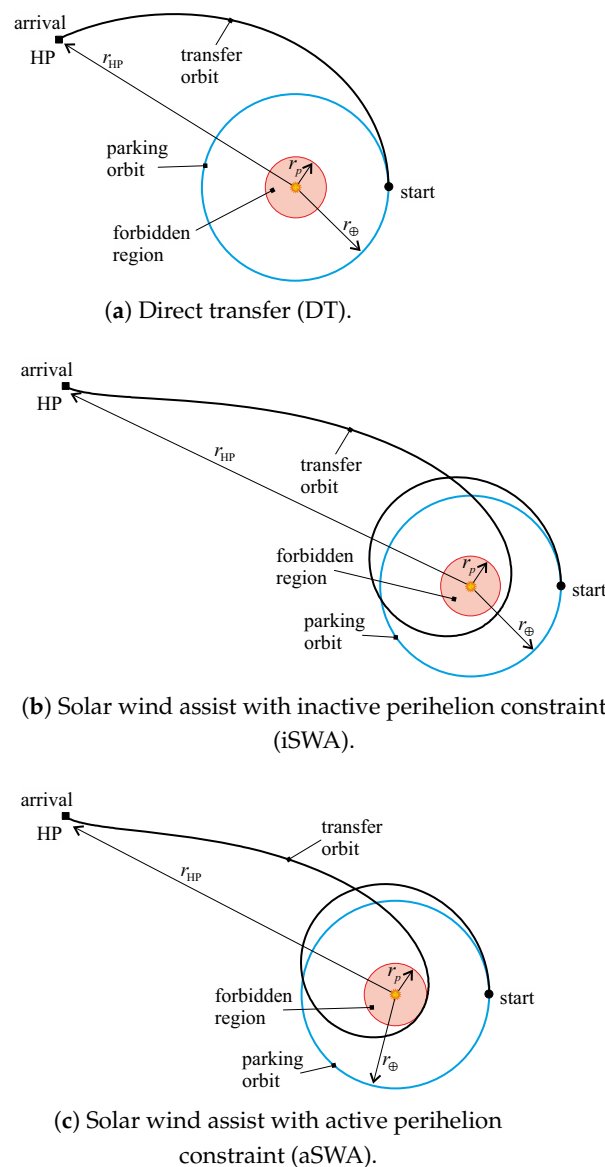


**Figure 5.** Three types of optimal transfer to HP in a simplified two-dimensional scenario.

### 3.1. Two-Dimensional Trajectory

The transfer performance is initially estimated by simulating a two-dimensional mission case in which the HP lies on the ecliptic (i.e.,  $h_{\text{HP}} \equiv 0$  au), and the ecliptic latitude of the target equilibrium point is  $\phi_{\text{HP}} = 0$  deg. In this simplified case, the design parameter reduces to the target solar distance, which was selected to be in the range  $r_{\text{HP}} \in [2, 8]$  au. The numerical results—that is, the minimum flight time as a function of the Sun–HP distance—are sketched in Figure 6.

The simulations show that an interplanetary transfer toward a HP with a medium-performance propulsion system (i.e., an E-sail with  $a_c = a_c^* = 1$  mm/s<sup>2</sup>) requires a flight time of about 5 years, while a high-performance E-sail with  $a_c = a_c^* = 3$  mm/s<sup>2</sup> needs a flight time of about 1.5 years.

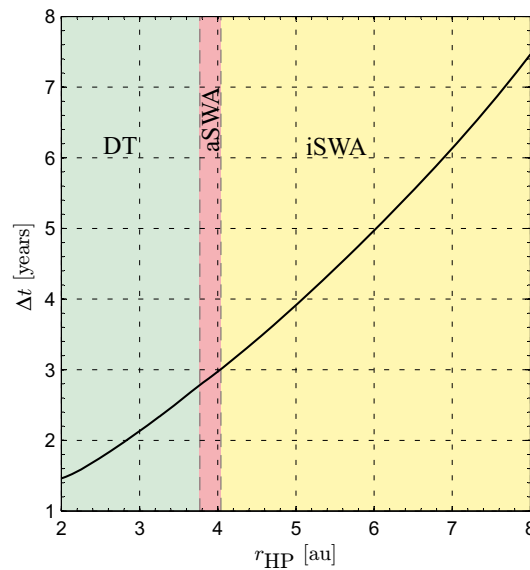


**Figure 6.** The minimum flight time as a function of the Sun–HP distance in a two-dimensional mission scenario.

Figure 6 also shows that a DT is obtained when the Sun–HP distance is below 3.77 au, that is, when the spacecraft characteristic acceleration is above 1.57 mm/s<sup>2</sup>; see also Figure 3. On the other hand, a SWA appears in the optimal trajectory when a medium-performance E-sail is considered with an active constraint (that is, an aSWA) in the range of  $a_c = a_c^* \in [1.47, 1.57]$  mm/s<sup>2</sup>, that is, when  $r_{\text{HP}} \in [3.77, 4]$  au. This behavior is consistent with the curve of Figure 7a, which shows the variation of the perihelion distance of the transfer trajectory with  $r_{\text{HP}}$  and with the optimal transfer trajectories sketched in Figure 8. Finally, the lines shown in Figure 7b, which report the final value of the ecliptic longitude  $\theta(t_f)$ , define the position of the HP on the ecliptic.

### 3.2. Three-Dimensional Scenario

In a more general three-dimensional case, the position of the HP target is identified by the pair  $\{r_{\text{HP}}, \phi_{\text{HP}}\}$ , so that the minimum flight time  $\Delta t$  is now a function of two independent design parameters—that is,  $\{r_{\text{HP}}, \phi_{\text{HP}}\}$ . Due to the problem symmetry with respect to the ecliptic (see Figure 2) without loss of generality, we assume  $\phi_{\text{HP}} \in [0, 90]$  deg, where the special case of  $\phi_{\text{HP}} = 0$  deg (or  $\phi_{\text{HP}} = 90$  deg) corresponds to a target HP point on the ecliptic (or exactly above the Sun’s north pole).

To reduce the number of simulations, three different values of the Sun–HP distance are considered, i.e.,  $r_{\text{HP}} \in \{2.5, 3, 3.5\}$  au, with a required characteristic acceleration of  $a_c = a_c^* \in \{2.37, 1.97, 1.69\}$  mm/s<sup>2</sup>, respectively. In the selected range of  $a_c^*$ , a DT is first simulated to facilitate the numerical convergence of the optimization procedure. Figure 9a,b show the flight time and the final ecliptic longitude as a function of the HP ecliptic latitude.

Note, in particular, that the values of  $\{\Delta t, \theta(t_f)\}$  when  $\phi_{HP} = 0$  deg are consistent with those obtained in the two-dimensional mission case; see Figures 6 and 7b.

The transfer trajectories when  $r_{HP} = 3$  au are sketched in Figure 10 for a set of values of  $\phi_{HP}$  to better emphasize the change in the transfer trajectory shape with  $\phi_{HP}$ . The special trajectory reported in Figure 10f shows the transfer toward a polar HP—a stationary point exactly above the Sun’s north pole. A potential mission application that requires the transfer toward such a vantage point for solar observation purposes is discussed in the next section.

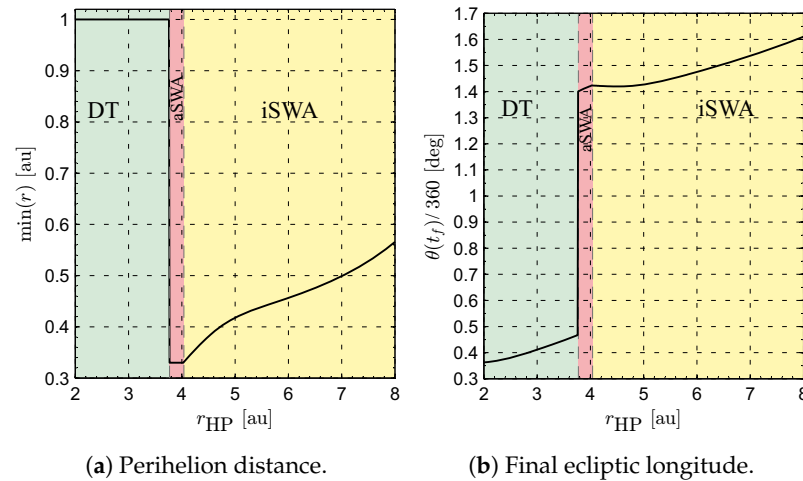


Figure 7. Optimal transfer trajectory characteristics as a function of  $r_{HP}$  in a two-dimensional mission scenario.

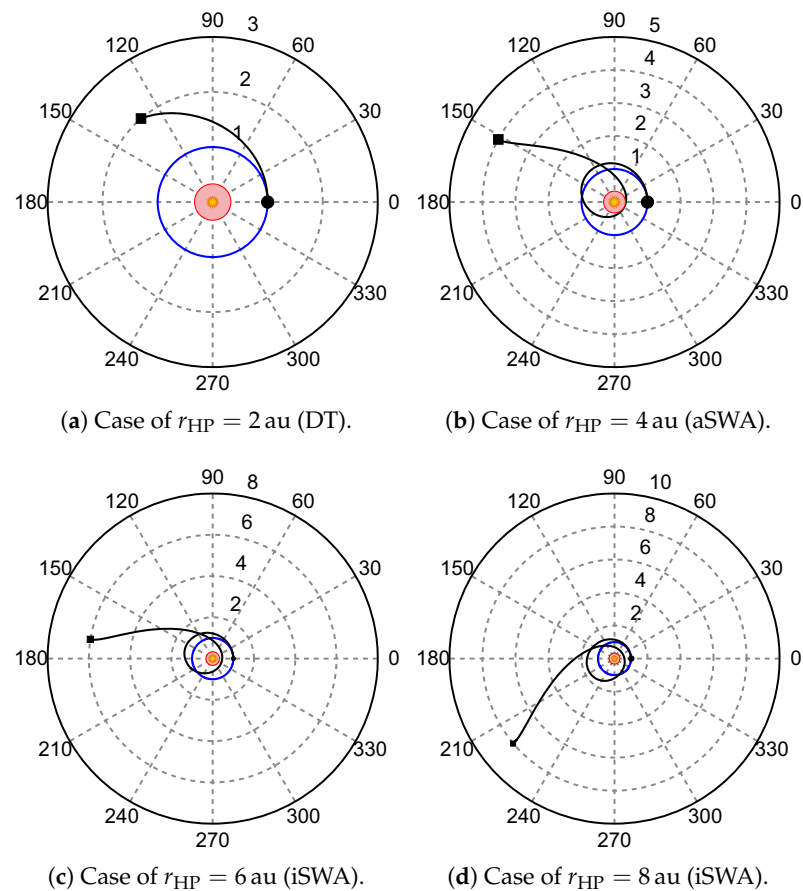
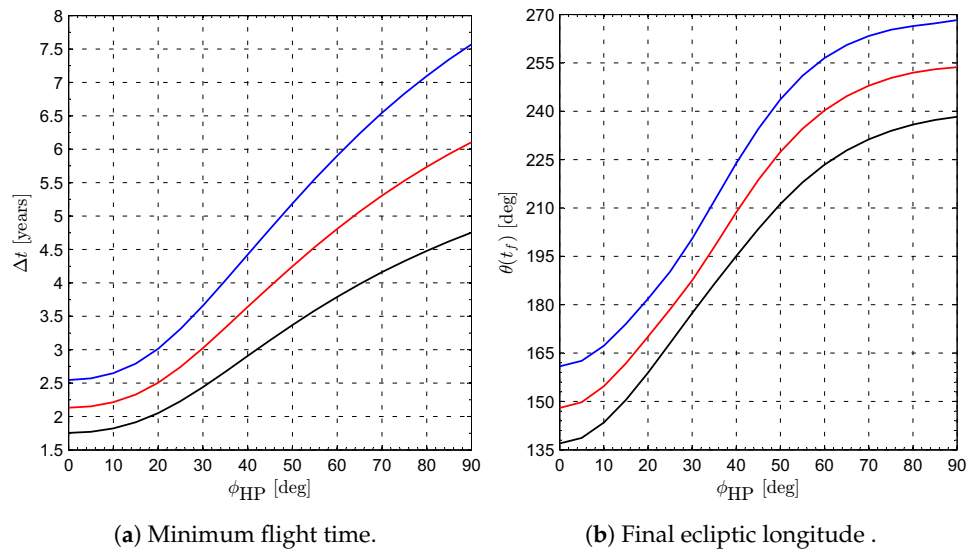
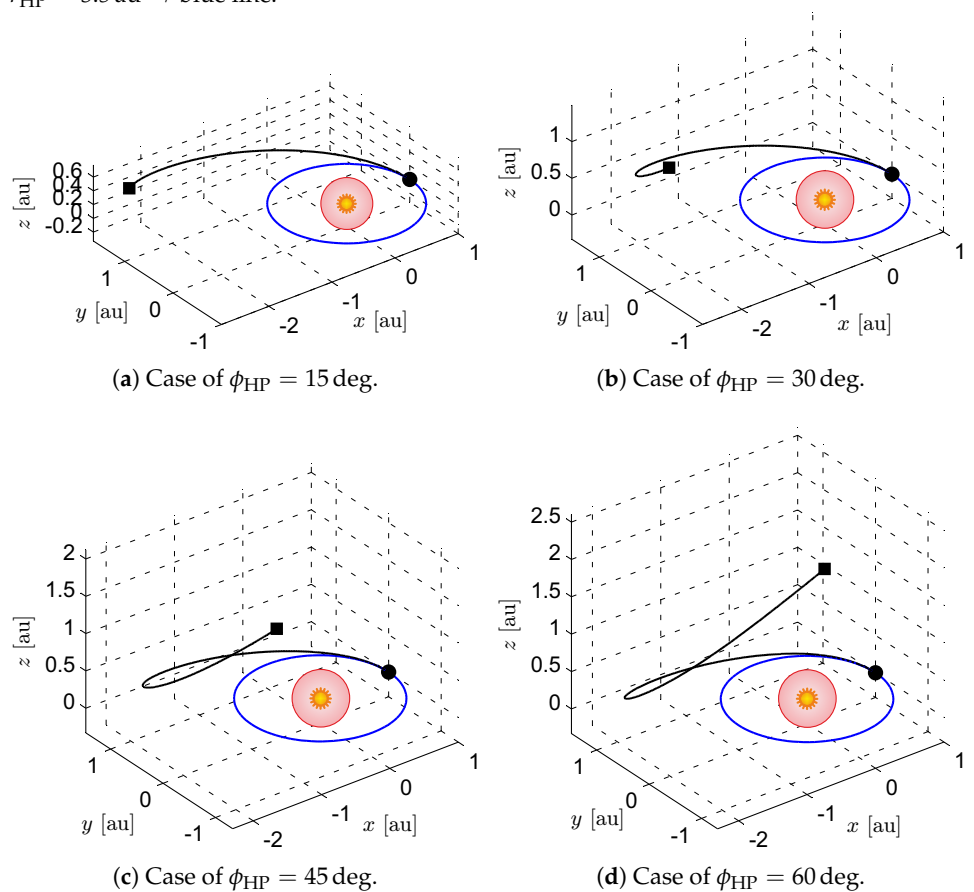


Figure 8. Optimal transfer trajectories in a two-dimensional mission scenario when  $r_{HP} \in \{2, 4, 6, 8\}$  au. The radial distance is in astronomical units, black circle  $\rightarrow$  start, and black square  $\rightarrow$  arrival/equilibrium point.



**Figure 9.** Minimum flight time and final ecliptic longitude as a function of the HP ecliptic latitude in a three-dimensional mission scenario with  $r_{HP} = 2.5$  au  $\rightarrow$  black line,  $r_{HP} = 3$  au  $\rightarrow$  red line, and  $r_{HP} = 3.5$  au  $\rightarrow$  blue line.



**Figure 10.** *Cont.*

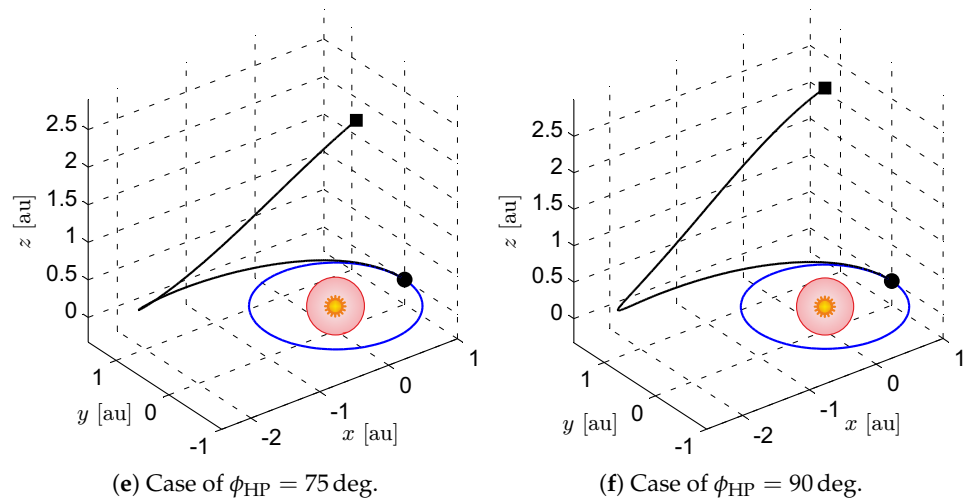


**Figure 10.** Optimal DT trajectories in a three-dimensional mission scenario as a function of  $\phi_{HP}$  when  $r_{HP} = 3$  au. Black circle  $\rightarrow$  start, and black square  $\rightarrow$  arrival/equilibrium point.

### 3.3. Mission Application

Consider a three-dimensional mission scenario in which the E-sail-based spacecraft reaches a polar HP (a point with  $\phi_{HP} = 90$  deg) placed at a distance  $r_{HP} \in [2, 3.5]$  au. In that case, the numerical simulations give the variation of the optimal flight time  $\Delta t$  with the final solar distance  $r_{HP}$  as shown in Figure 11a. The mission time increases nearly linearly with the target distance  $r_{HP}$ . The optimal transfer trajectories are illustrated in Figure 11b. From the simulation results, we found that a polar HP at a solar distance of 3 au can be reached within about 6 years, while a distance of 2.5 au is reached in less than 5 years. In the latter case, that is, when  $r_{HP} = 2.5$  au, the time variations of the three control variables  $\{\tau, \alpha, \delta\}$  are sketched in Figure 12.

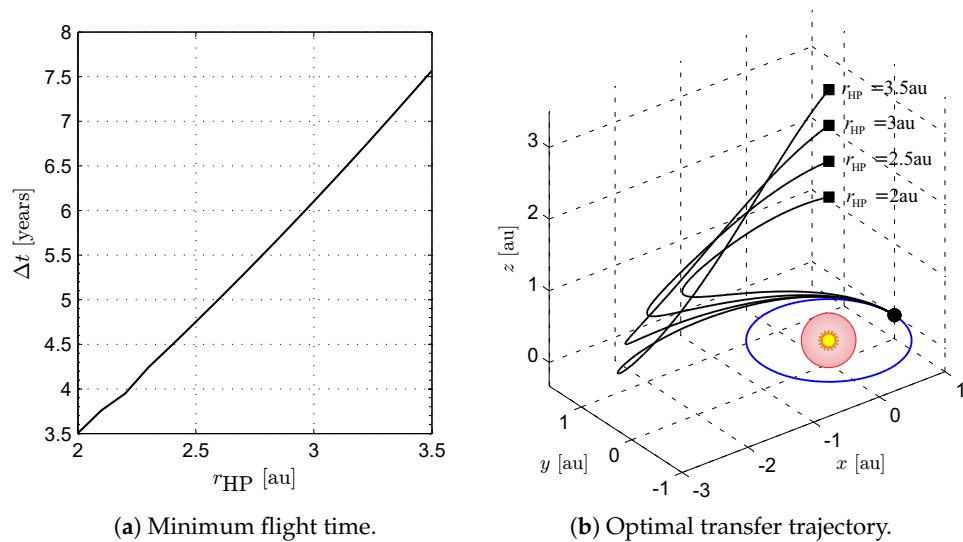


**Figure 11.** The minimum flight time and optimal transfer trajectory to reach a polar HP as a function of the solar distance.

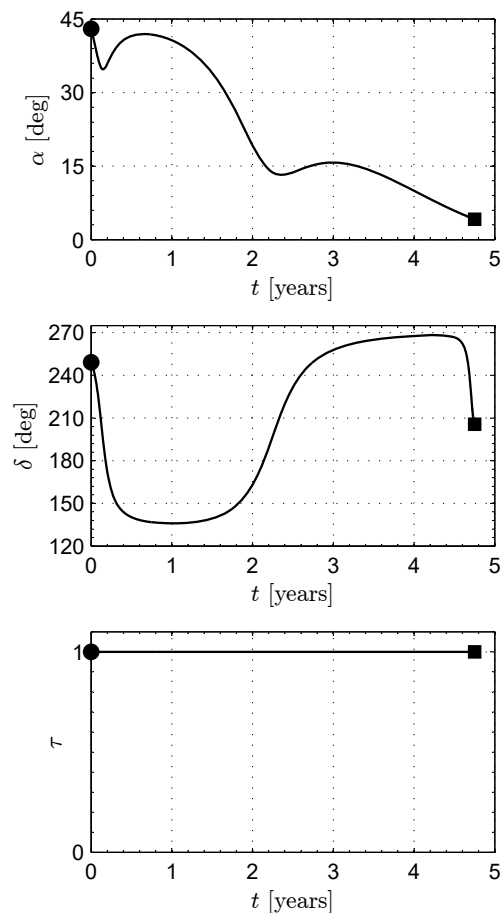


**Figure 12.** Tie variation of the control variables  $\{\tau, \alpha, \delta\}$  when  $r_{HP} = 2.5$  au. Black circle  $\rightarrow$  start, and black square  $\rightarrow$  arrival/equilibrium point.

#### 4. Conclusions

In this paper, we analyzed the performance of an E-sail-based spacecraft in an interplanetary transfer toward a heliocentric equilibrium point. The peculiarity of the E-sail thrust concept allows for a heliostationary point to be reached by a probe propelled by a medium-performance propulsion system. This is particularly true when the heliostationary point is sufficiently far from the Sun. For example, a spacecraft with a propulsive acceleration equal to  $1 \text{ mm/s}^2$  is able to maintain a static equilibrium point placed on the Ecliptic at about 6 astronomical units from the Sun and to reach it within a transfer time of about 5 years.

The required E-sail performance increases as the equilibrium point heliocentric distance reduces. Even though a heliostationary point at a solar distance of 2 astronomical units needs a high performance E-sail, the required characteristic acceleration, equal to about  $3 \text{ mm/s}^2$ , is well below the value (roughly equal to  $6 \text{ mm/s}^2$ ) needed to maintain the same point by means of a photonic solar sail. Nevertheless, a fair comparison between these two propulsion concepts in such an advanced mission scenario is not so simple and requires a more accurate mission analysis, which is beyond the scope of this paper. In particular, the comparison should include a mass breakdown scheme and a mathematical model able to quantify the interactions between the main trajectory characteristics (perihelion distance and flight time) and the mission design parameters, such as the heliostationary point position and the spacecraft subsystem masses, including the payload.

**Author Contributions:** Conceptualization, A.A.Q.; methodology, A.A.Q.; software, A.A.Q.; writing—original draft preparation, A.A.Q. and G.M.; writing—review and editing, G.M. All authors have read and agreed to the published version of the manuscript.

**Funding:** This work was partly supported by the University of Pisa, Progetti di Ricerca di Ateneo (Grant no. PRA\_2022\_1).

**Institutional Review Board Statement:** Not applicable.

**Informed Consent Statement:** Not applicable.

**Data Availability Statement:** Not applicable.

**Conflicts of Interest:** The authors declare no conflict of interest.

## Abbreviations

The following abbreviations are used in this manuscript:

$a_c$	characteristic acceleration [mm/s <sup>2</sup> ]
$a_r$	radial component of $\mathbf{a}$ [mm/s <sup>2</sup> ]
$a_\theta$	transverse component of $\mathbf{a}$ [mm/s <sup>2</sup> ]
$a_\phi$	azimuthal component of $\mathbf{a}$ [mm/s <sup>2</sup> ]
$\mathbf{a}$	propulsive acceleration vector [mm/s <sup>2</sup> ]
$\mathcal{H}$	Hamiltonian function
$h$	distance from the ecliptic [au]
$\hat{\mathbf{i}}_r$	radial unit vector
$\hat{\mathbf{i}}_\theta$	transverse unit vector
$\hat{\mathbf{i}}_\phi$	azimuthal unit vector
$J$	performance index [days]
$O$	Sun's center of mass
$r$	radial distance [au]
$r_p$	minimum perihelion radius [au]
$r_\oplus$	reference distance [1 au]
$S_w$	switching function
$t$	time [days]
$\mathcal{T}(O; r, \theta, \phi)$	spherical reference frame
$\mathcal{T}_S(O; x, y, z)$	heliocentric-ecliptic reference frame
$v_r$	radial component of the spacecraft velocity vector [km/s]
$v_\theta$	transverse component of the spacecraft velocity vector [km/s]
$v_\phi$	azimuthal component of the spacecraft velocity vector [km/s]
$\alpha$	sail cone angle [rad]
$\Delta t$	flight time [days]
$\delta$	sail clock angle [rad]
$\theta$	ecliptic longitude [rad]
$\lambda_r$	variable adjoint to $r$
$\lambda_\theta$	variable adjoint to $\theta$
$\lambda_\phi$	variable adjoint to $\phi$
$\lambda_{v_r}$	variable adjoint to $v_r$
$\lambda_{v_\theta}$	variable adjoint to $v_\theta$
$\lambda_{v_\phi}$	variable adjoint to $v_\phi$
$\mu_\odot$	Sun's gravitational parameter [km <sup>3</sup> /s <sup>2</sup> ]
$\tau$	dimensionless switching parameter
$\phi$	ecliptic latitude [rad]
<i>Subscripts</i>	
0	initial, parking orbit
$f$	final
HP	heliostationary point
$p$	perihelion
<i>Superscripts</i>	
$\cdot$	derivative with respect to time
$'$	function of control variables

### Appendix A

This Appendix describes the mathematical model used to evaluate the minimum time transfer trajectories, that is, the trajectories that maximize the performance index

$$J \triangleq -\Delta t \equiv -t_f. \tag{A1}$$

According to the general approach described in the classic textbook by Bryson and Ho [35], and bearing in mind the equations of motion (6)–(11), the maximum of  $J$  is obtained by constructing the Hamiltonian function

$$\mathcal{H} \triangleq \lambda_r \dot{r} + \lambda_\theta \dot{\theta} + \lambda_\phi \dot{\phi} + \lambda_{v_r} \dot{v}_r + \lambda_{v_\theta} \dot{v}_\theta + \lambda_{v_\phi} \dot{v}_\phi \tag{A2}$$

where  $\lambda_i$  is the (generic) variable adjoint to the  $i$ -th state variable, with  $i \in \{r, \theta, \phi, v_r, v_\theta, v_\phi\}$ . The time derivative of  $\lambda_i$  is obtained from the Euler–Lagrange equations

$$\dot{\lambda}_i = -\frac{\partial \mathcal{H}}{\partial i} \quad \text{with} \quad i \in \{r, \theta, \phi, v_r, v_\theta, v_\phi\} \tag{A3}$$

The calculation of an explicit expression for the six Euler–Lagrange equations is straightforward and is omitted here for the sake of brevity.

Taking Equation (5) into account, we note that the part  $\mathcal{H}'$  of the Hamiltonian function that explicitly depends on the controls  $\{\tau, \alpha, \delta\}$  is

$$\mathcal{H}' \triangleq \lambda_{v_r} a_r + \lambda_{v_\theta} a_\theta + \lambda_{v_\phi} a_\phi, \tag{A4}$$

that is,

$$\mathcal{H}' = \tau \frac{a_c r_\oplus}{2r} \left[ \lambda_{v_r} (1 + \cos \alpha^2) + \lambda_{v_\theta} \cos \alpha \sin \alpha \cos \delta + \lambda_{v_\phi} \cos \alpha \sin \alpha \sin \delta \right] \tag{A5}$$

According to the Pontryagin’s maximum principle, and using the general results from Ref. [21], we find the expressions of the control  $\{\tau, \alpha, \delta\}$  that maximize, at any time, the function  $\mathcal{H}'$  (and thus the Hamiltonian function  $\mathcal{H}$ ), that is,

$$\cos \delta = \frac{\lambda_{v_\theta}}{\sqrt{\lambda_{v_\theta}^2 + \lambda_{v_\phi}^2}}, \quad \sin \delta = \frac{\lambda_{v_\phi}}{\sqrt{\lambda_{v_\theta}^2 + \lambda_{v_\phi}^2}} \tag{A6}$$

$$\cos 2\alpha = \frac{\lambda_{v_r}}{\sqrt{\lambda_{v_\theta}^2 + \lambda_{v_\phi}^2 + \lambda_{v_r}^2}}, \quad \sin 2\alpha = \frac{\sqrt{\lambda_{v_\theta}^2 + \lambda_{v_\phi}^2}}{\sqrt{\lambda_{v_\theta}^2 + \lambda_{v_\phi}^2 + \lambda_{v_r}^2}} \tag{A7}$$

$$\tau = \frac{1 + \text{sign}(S_w)}{2} \tag{A8}$$

where  $\text{sign}(\square)$  is the signum function, and  $S_w$  is a switching function defined as

$$S_w \triangleq \lambda_{v_r} (1 + \cos \alpha^2) + \lambda_{v_\theta} \cos \alpha \sin \alpha \cos \delta + \lambda_{v_\phi} \cos \alpha \sin \alpha \sin \delta \tag{A9}$$

in which the two angles  $\alpha$  and  $\delta$  are obtained from Equations (A6) and (A7), respectively.

The differential system of 12 nonlinear equations is given by the 6 equations of motion (6)–(11) and the 6 Euler–Lagrange Equations (A3). Recalling that the flight time  $t_f$  is an output of the optimization process [35], and assuming a DT or an iSWA, the 13 boundary (scalar) conditions that complete the two-point boundary value problem (TPBVP) are given by Equations (12) and (13) and the transversality condition [35], that is

$$\lambda_\theta(t_f) = 0 \quad , \quad \mathcal{H}(t_f) = 1 \tag{A10}$$

When, instead, an aSWA occurs, that is, if an interior point constraint appears in the optimization process, only the adjoint variable  $\lambda_r$  has an impulsive variation at the point where the transfer trajectory becomes tangent to the circular forbidden zone (time  $t = t_1 \in (t_0, t_f)$ ). In the latter case, the values of  $t_1$  and the jump of  $\lambda_r$  at  $t_1$  are obtained by enforcing the two tangency conditions

$$r(t_1) = r_p \quad , \quad v_r(t_1) = 0 \quad (\text{A11})$$

The TPBVP associated with the optimization process is solved, with an absolute error less than  $10^{-8}$ , through a hybrid numerical technique that combines a genetic algorithm to obtain a first estimate of the unknown adjoint variables, with gradient-based and direct methods to refine the solution. A continuation procedure is used to improve the convergence process and reduce the computation time.

## References

1. Forward, R.L. Statite—A spacecraft that does not orbit. *J. Spacecr. Rocket.* **1991**, *28*, 606–611. [[CrossRef](#)]
2. Ceriotti, M.; Diedrich, B.L.; McInnes, C.R. Novel mission concepts for polar coverage: An overview of recent developments and possible future applications. *Acta Astronaut.* **2012**, *80*, 89–104. [[CrossRef](#)]
3. Ceriotti, M.; Heiligers, J.; McInnes, C.R. Trajectory and Spacecraft Design for a Pole-Sitter Mission. *J. Spacecr. Rocket.* **2014**, *51*, 311–326. [[CrossRef](#)]
4. McInnes, C.R. Inverse Solar Sail Trajectory Problem. *J. Guid. Control. Dyn.* **2003**, *26*, 369–371. [[CrossRef](#)]
5. McKay, R.J.; Macdonald, M.; Biggs, J.; McInnes, C. Survey of Highly Non-Keplerian Orbits with Low-Thrust Propulsion. *J. Guid. Control Dyn.* **2011**, *34*, 645–666. [[CrossRef](#)]
6. McInnes, C.R.; McDonald, A.J.C.; Simmons, J.F.L.; MacDonald, E.W. Solar sail parking in restricted three-body systems. *J. Guid. Control Dyn.* **1994**, *17*, 399–406. [[CrossRef](#)]
7. Mengali, G.; Quarta, A.A. Optimal heliostationary missions of high-performance sailcraft. *Acta Astronaut.* **2007**, *60*, 676–683. [[CrossRef](#)]
8. Quarta, A.A.; Mengali, G.; Niccolai, L. Solar Sail Optimal Transfer Between Heliostationary Points. *J. Guid. Control Dyn.* **2020**, *43*, 1935–1942. [[CrossRef](#)]
9. Fu, B.; Sperber, E.; Eke, F. Solar sail technology—A state of the art review. *Prog. Aerosp. Sci.* **2016**, *86*, 1–19. [[CrossRef](#)]
10. Gong, S.; Macdonald, M. Review on solar sail technology. *Astrodynamics* **2019**, *3*, 93–125. [[CrossRef](#)]
11. Dachwald, B.; Mengali, G.; Quarta, A.A.; Macdonald, M. Parametric model and optimal control of solar sails with optical degradation. *J. Guid. Control Dyn.* **2006**, *29*, 1170–1178. [[CrossRef](#)]
12. Davoyan, A.R.; Munday, J.N.; Tabiryan, N.; Swartzlander, G.A.; Johnson, L. Photonic materials for interstellar solar sailing. *Optica* **2021**, *8*, 722–734. [[CrossRef](#)]
13. Bruno, C.; Accettura, A.G.; Seboldt, W.; Dachwald, B. *Advanced Propulsion Systems and Technologies, Today to 2020*; American Institute of Aeronautics and Astronautics: Reston, VA, USA 2008; Chapter 1, 16, pp. 1–18. 427–452. [[CrossRef](#)]
14. Vilela Salgado, M.C.; Neyra Belderrain, M.C.; Campos Devezas, T. Space Propulsion: A Survey Study About Current and Future Technologies. *J. Aerosp. Technol. Manag.* **2018**, *10*, 1–23. [[CrossRef](#)]
15. Janhunen, P.; Toivanen, P.K.; Polkko, J.; Merikallio, S.; Salminen, P.; Haeggström, E.; Seppänen, H.; Kurppa, R.; Ukkonen, J.; Kiprich, S.; et al. Electric solar wind sail: Toward test missions. *Rev. Sci. Instrum.* **2010**, *81*, 111301–1–11301–11. [[CrossRef](#)] [[PubMed](#)]
16. Janhunen, P. Electric sail for spacecraft propulsion. *J. Propuls. Power* **2004**, *20*, 763–764. [[CrossRef](#)]
17. Janhunen, P.; Sandroos, A. Simulation study of solar wind push on a charged wire: Basis of solar wind electric sail propulsion. *Ann. Geophys.* **2007**, *25*, 755–767. [[CrossRef](#)]
18. Bassetto, M.; Nicolai, L.; Quarta, A.A.; Mengali, G. A comprehensive review of Electric Solar Wind Sail concept and its applications. *Prog. Aerosp. Sci.* **2022**, *128*, 1–27. [[CrossRef](#)]
19. Janhunen, P.; Toivanen, P.; Envall, J.; Slavinskis, A. Using charged tether Coulomb drag: E-sail and plasma brake. In Proceedings of the Fifth International Conference on Tethers in Space, Ann Arbor, MI, USA, 24–26 May 2016.
20. Toivanen, P.K.; Janhunen, P. Thrust vectoring of an electric solar wind sail with a realistic sail shape. *Acta Astronaut.* **2017**, *131*, 145–151. [[CrossRef](#)]
21. Huo, M.Y.; Mengali, G.; Quarta, A.A. Electric sail thrust model from a geometrical perspective. *J. Guid. Control Dyn.* **2018**, *41*, 735–741. [[CrossRef](#)]
22. Bassetto, M.; Mengali, G.; Quarta, A.A. Stability and control of spinning E-sail in heliostationary orbit. *J. Guid. Control Dyn.* **2019**, *42*, 425–431. [[CrossRef](#)]
23. Bate, R.R.; Mueller, D.D.; White, J.E. *Fundamentals of Astrodynamics*; Dover Publications: New York, NY, USA, 1971; Chapter 2, pp. 53–55.

24. Merikallio, S.; Janhunen, P. The electric solar wind sail (E-sail): Propulsion innovation for solar system travel. *Bridge* **2018**, *48*, 28–32.
25. Wiegmann, B.M. Conceptual Design of an Electric Sail Technology Demonstration Mission Spacecraft. In Proceedings of the 40th Annual AAS Rocky Mountain Section Guidance and Control Conference, Breckenridge, CO, USA, 2–8 February 2017.
26. Mengali, G.; Quarta, A.A.; Janhunen, P. Electric sail performance analysis. *J. Spacecr. Rocket.* **2008**, *45*, 122–129. [[CrossRef](#)]
27. Quarta, A.A.; Mengali, G.; Bassetto, M.; Niccolai, L. Optimal circle-to-ellipse orbit transfer for Sun-facing E-sail. *Aerospace* **2022**, *9*, 671. [[CrossRef](#)]
28. Niccolai, L.; Quarta, A.A.; Mengali, G.; Bassetto, M. Trajectory analysis of a zero-pitch angle E-sail with homotopy perturbation technique. *J. Guid. Control Dyn.* **2023**, *in press*. [[CrossRef](#)]
29. Mengali, G.; Quarta, A.A.; Aliasi, G. A graphical approach to electric sail mission design with radial thrust. *Acta Astronaut.* **2013**, *82*, 197–208. [[CrossRef](#)]
30. Quarta, A.A.; Mengali, G. Analysis of electric sail heliocentric motion under radial thrust. *J. Guid. Control Dyn.* **2016**, *39*, 1431–1435. [[CrossRef](#)]
31. Janhunen, P.; Quarta, A.A.; Mengali, G. Electric solar wind sail mass budget model. *Geosci. Instrum. Methods Data Syst.* **2013**, *2*, 85–95. [[CrossRef](#)]
32. Wie, B. Thrust Vector Control Analysis and Design for Solar-Sail Spacecraft. *J. Spacecr. Rocket.* **2007**, *44*, 545–557. [[CrossRef](#)]
33. Mengali, G.; Quarta, A.A. Non-Keplerian orbits for electric sails. *Celest. Mech. Dyn. Astron.* **2009**, *105*, 179–195. [[CrossRef](#)]
34. Quarta, A.A.; Mengali, G. Electric sail mission analysis for outer solar system exploration. *J. Guid. Control Dyn.* **2010**, *33*, 740–755. [[CrossRef](#)]
35. Bryson, A.E.J.; Ho, Y.C. *Applied Optimal Control*; Taylor & Francis Group: New York, NY, USA, 1975.
36. Leipold, M.; Wagner, O. ‘Solar photonic assist’ trajectory design for solar sail missions to the outer solar system and beyond. In Proceedings of the AAS/GSFC International Symposium on Flight Dynamics, Greenbelt, MD, USA, 11–15 May 1998.

**Disclaimer/Publisher’s Note:** The statements, opinions and data contained in all publications are solely those of the individual author(s) and contributor(s) and not of MDPI and/or the editor(s). MDPI and/or the editor(s) disclaim responsibility for any injury to people or property resulting from any ideas, methods, instructions or products referred to in the content.